energies

Article

Numerical Analysis of Induced Steady Flow on a Bus

Ferenc Szodrai

Department of Building Services and Building Engineering, Faculty of Engineering, University of Debrecen, 4028 Debrecen, Hungary; szodrai@eng.unideb.hu

Abstract: Buses are large vehicles with the primary goal of carrying as many passengers as possible while maintaining a comfortable interior and an economical driving cycle. With various adjustments, small changes can add up to significant energy savings. This study investigates the issue of whether there is a scenario in which the enormous power demand needed for the operation of buses can be reduced by some amount. Large eddy simulation was used for this analysis, which was carried out using commercially available software. The external unit was located on the front and rear ends of the roof of the bus, as well as in the rear. The findings suggest that the current position of the unit can be improved, and the aerodynamic losses can be increased or decreased, depending on the position of the induced flow.

Keywords: bus; large eddy simulation; drag reduction; aerodynamic analysis; side-view mirrors

Citation: Szodrai, F. Numerical Analysis of Induced Steady Flow on a Bus. *Energies* **2022**, *15*, 8444. https://doi.org/10.3390/en15228444

Academic Editors: Ishak Bin Hashim, Hussein A. Z. AL-bonsrulah, Dhinakaran Veeman and Mogalahalli V. Reddy

Received: 29 October 2022
Accepted: 9 November 2022
Published: 11 November 2022

1. Introduction

Energy consumption reduction is becoming increasingly pivotal nowadays. One of the major power losses in public transportation comes from the external air conditioning unit (AC) used to maintain a satisfactory level of comfort. A vehicle becomes more energy-efficient when it lacks a ventilation system [1]. Without an appropriate ventilation system, the risk of exposure to air contaminants from road traffic [2] or airborne virus transmission [3,4] rises.

The positioning of the external unit of the AC has a large degree of freedom. Because of the ease of its installation, it is commonly installed on the roof of the bus; however, the longitudinal location might vary, depending on the kind of bus.

The primary goal of this research was to determine whether there was an advantageous position for the AC in terms of reducing aerodynamic loss. This task is mostly an evaluation of a passive system in which the position of a "bump", i.e., AC, varies. However, fans are necessary to remove or add heat from the cycle, resulting in a continuous flow induction in the near-wall zone. This might change the amount of aerodynamic loss experienced by the vehicle. Despite this, no research on steady flow injection from the roof of a vehicle has been found. Usually, when the flow is induced from the roof, it is pulsating [5,6].

Although injecting flow from the rear surface of the vehicle is an advantageous method to reduce drag [7], it is possible to achieve the same phenomenon passively by constructing a pipe system that transmits flow from the frontal zone [8]. Alternatively, active systems with higher flow rates can provide greater loss reduction [9–11]. There are studies investigating pulsating flow systems; however, because of the continuous flow from the axial fan, the oscillations may be ignored in the current investigation.

This study is a continuation of aerodynamic research in which first drag reduction was assessed [7], and then the aerodynamics of an urban bus was modelled [12]; finally, in this study, a drag-reduction solution is proposed for urban buses. Based on the previous numerical evaluation, a more detailed model depicts the most typical cruising condition of a bus in the city of Debrecen.

To start with, the bus model was made using schematics provided by the Debrecen Public Transport Company (DKV Ltd.), and then the aerodynamic behaviours were analysed by applying large eddy simulations.

2. Materials and Methods

The core concept was that an induced steady flow may disrupt the flow around a blunt vehicle, hence changing the drag force applied to it. The AC is the source of the constant flow, because the position of the AC may be arbitrarily located anywhere on the bus. It was expected that this work would aid in prioritizing its location. Three design solutions were investigated.

2.1. Geometry

The geometries (see Figure 1a) were based on the type Mercedes-Benz Reform 501 LE bus, the sketch of which was provided by DKV Ltd. The base dimension in the domain was the total height of the vehicle H = 3280 mm. This bus was investigated in a previous study [12] in side-wind conditions.

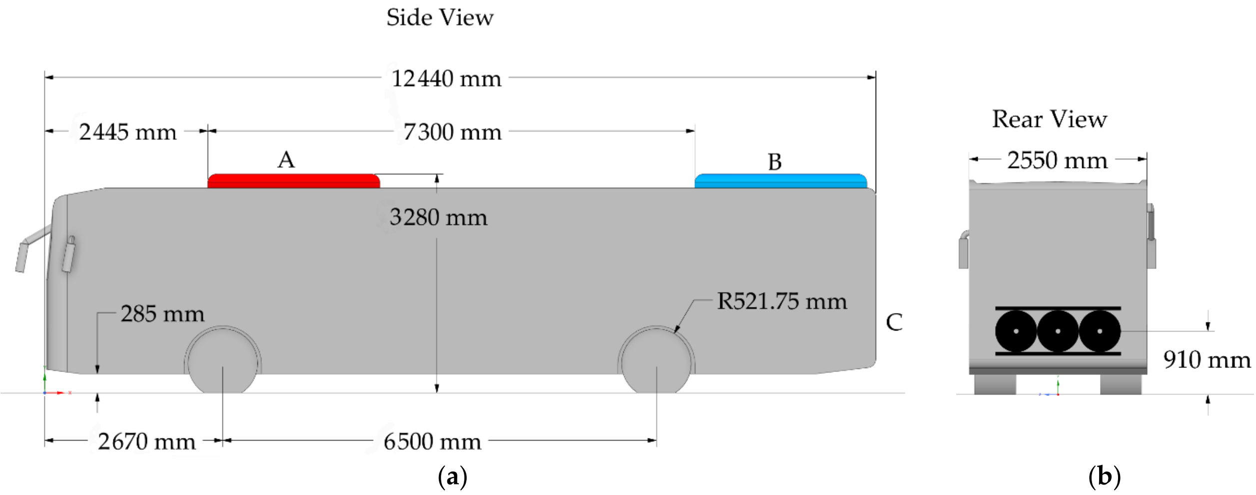

Figure 1. Schematic of the bus (**a**) side and (**b**) rear view.

Two further modifications to the initial geometry were evaluated. Figure 1 depicts the combination of the geometries. The first (model A) was based on the "original" design, with the AC located at the front edge of the roof, as indicated in red. The AC in the second (model B) was shifted 7300 mm to the rear edge (indicated in blue). In the third (model C) design, the AC was removed, and it was hypothetically positioned in the engine section at the bottom rear section (see Figure 1b).

The side-view mirrors were additions to the geometry seen in Figure 1a. Previously, they were not modelled for the following reasons: the side view mirror design was asymmetrical, but for side-wind assessment a symmetrical shape was required; for urban buses, the design of these mirrors can have a wide range of variation, and in some wind tunnel measurements, the small-scale model lacks the mirrors [13,14].

To ensure acceptable visibility, the mirrors on the entry side of urban buses are bigger, and placed further away from the bus. The vertical position of mirrors might vary, although on the most frequent variant of this bus it is a fixed position. The mirror on the other side is attached to the corner edge.

When heating is required in the bus, the AC extracts heat from outside, and when cooling is required, it removes heat to the outside of the bus. A high flow rate is required for a small unit to be effective. According to the data provided, the type SPHEROS REVO 360 flows 6960 $m^3 \cdot h^{-1}$ of air via a heat exchanger with three axial fans (see Figure 2a).

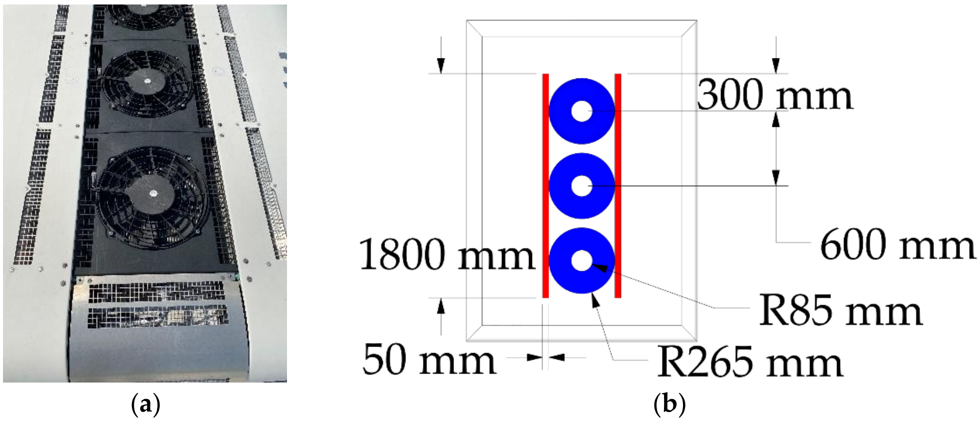

Figure 2. Openings of the air conditioning unit (**a**) photo and (**b**) schematic.

Figure 2a shows that grills are arranged radially for protection. These grills were small, which is why they were disregarded when the area of boundary criteria was set, but they were large enough to negate the majority of the swirls produced by the spinning rotors.

The dimensions of the digital wind tunnel were as follows: length 20 H, width 9 H, and height 5 H; the bus was placed 5 H in front of the inlet. To depict more accurately the flow, a one-metre-thick refinement zone was also added at the sides and top of the bus (see Figure 3). Since the wake region was large at the rear end, a 1 H long extension was added to the refinement zone.

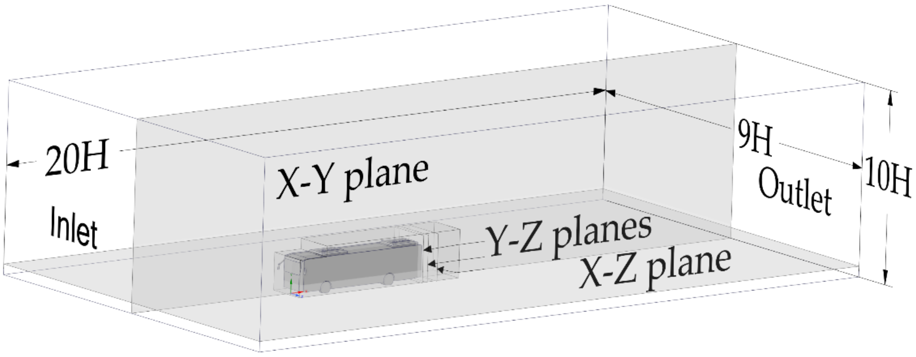

Figure 3. Flow domain of the bus.

From the geometry file of the bus, the frontal projected area was determined. The frontal projected area of the bus was different; without mirrors (previous study [12]) $A_0 = 7.80\ m^2$; for model A and B, when there were side-view mirrors $A_{A;B} = 7.975\ m^2$; and without the top AC unit $A_r.579\ m^2$. For comparison, the frontal projected area was always the corresponding area to the model, and not a baseline area.

2.2. Mesh

After the geometry had been defined the simulation was carried out with ANSYS Fluent 2022 R1 (ANSYS Inc., Canonsburg, PA, USA) software. Many steps of discretisation were taken from the previous study [12].

Three types of cells were used: a hexagonal one for the core domain, a prismatic one for the near-wall zones, and, for transition between the two types of mesh, a polyhedral one. The created mesh was not homogeneous. Table 1 shows two kinds of first layer heights (y_H) and the maximum cell size (Δ_{max}) used. The main idea of the mesh structure was to create an optimized solution which has a low cell count, yet provides accurate results. The $y_{H\,fine}$ and $\Delta_{max\,fine}$ constraints were applied on the frontal surface of the bus, on the wheels and on the mirrors.

Table 1. Mesh properties.

Cases	$y_{H\,fine}$	y_H	Δ_{min}	$\Delta_{max\,fine}$	Δ_{max}	Cell Count
Fine Mesh	0.1 mm	1 mm	20	40 mm	320 mm	8.6×10^6
Medium Mesh	0.2 mm	2 mm	40	80 mm	640 mm	1.8×10^6
Coarse Mesh	0.4 mm	4 mm	80	160 mm	1280 mm	0.4×10^6

For meshing, the following quality indicators were set: growth rate of 1.2, maximum skewness of 0.8, and minimum orthogonal quality of 0.1. The three created meshes had acceptable quality indicators (see Table 2), in line with the grid convergence index (GCI) [15]. The quality indicators were low at a few peaked spots, but this did not affect the accuracy of the model.

Table 2. Quality indicators.

Cases	Average Orthogonal	Average Skewness	Average Aspect Ratio	GCI
Fine Mesh	0.97	0.03	4.6	0.007%
Medium Mesh	0.96	0.04	5.3	-
Coarse Mesh	0.95	0.05	5.7	0.254%

The mesh independence analysis required the GCI. In model A, the drag force on the bus served as the control variable for the assessment. It should be mentioned that the standard deviation was also evaluated; however, it followed the same pattern as the mean force values (see Figure 4a). The coarse mesh differed significantly from the finer variants, although additional refining did not result in more accurate results when the scaling factor was two. Further simulations were carried out on the medium mesh, based on the aforementioned factors.

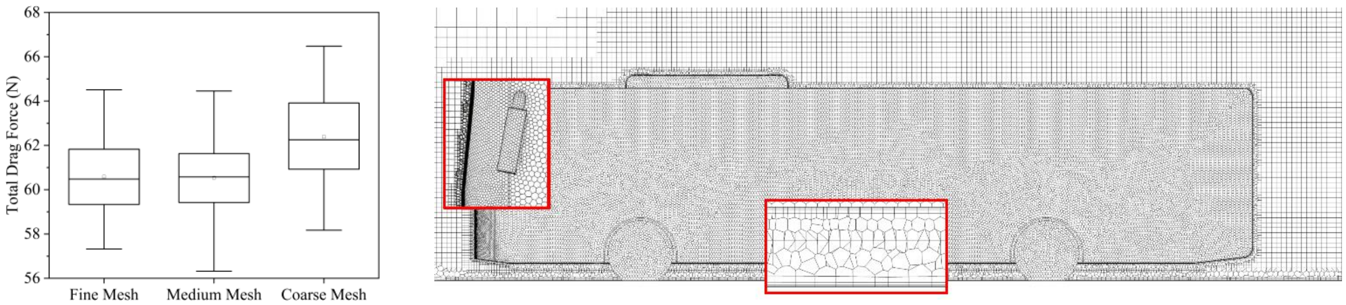

(**a**) (**b**)

Figure 4. (**a**) Mesh sensitivity results and (**b**) vertical cross-section view of the Medium Mesh.

Figure 4b depicts the mesh of model A using the medium mesh configuration. Both on the surface of the bus and on the ground, four layers of prismatic mesh were enough to depict the logarithmic layer of the near-wall boundary zone. The surface mesh size was ten times larger than y_H. It can also be seen that the relevant areas in Figure 4b (frontal side-view mirrors) had finer mesh. Because it was difficult to create hexahedral structured mesh between the bottom of the bus and the ground, the lower section was created by using polyhedral cells. In the upper left-hand corner of Figure 4b, one can see that the mesh size was larger, due to the optimized mesh structure.

2.3. Numerical Setup

For the aerodynamic study, the wall-adapting local eddy-viscosity large eddy simulation (WALE-LES) [16] approach was used. This method implies an unsteady solution method. To obtain an accurate model, the time step was adjusted to 0.01 s, which caused the residuals of the velocity components to rapidly converge to $10^{-5.5}$ magnitude. The flow developed in the first 10 s with the low time-step, and then an additional 50 s were simulated. Even when the AC was turned on, the speed from the digital wind tunnel had such a huge influence that the effects of natural convection ceased.

The computational setup was the same as in the previous study [12]. The model was isothermal, so for velocity and pressure-based solver, the semi-implicit method for a pressure-linked equations–consistent pressure–velocity coupling scheme was used. Furthermore, for pressure discretisation, PRESTO! was used, and for momentum and transient formulations, bounded central differencing was applied.

The primary flow speed in the digital wind tunnel was determined by the most common cruising speed (v_c) of the investigated bus [17]. This magnitude was rounded up to 20 km·h^{-1} in the simulation.

This speed was utilised to set the moving surface speed of the ground, the tyre surfaces, and the angular velocity of the rims. The solid surfaces were no-slip walls. The volume flow rate and air density (ρ = 1.225 kg·m^{-3}) were used to define the intake and exhaust flow of the AC. The volume flow rate was 6960 m^3·h^{-1}, and simulations were performed at 0%; 50% and 100% of this amount. The sides and top of the wind tunnel had free slip walls, implying that the symmetry condition was utilised. Flows exited through a pressure outlet. The boundary conditions are summarized in Table 3. Altogether, a total of 9 simulations were made for comparison.

Table 3. Boundary conditions.

Type	Magnitude	Comment
Inlet	20 km·h^{-1}	Velocity inlet
Ground	20 km·h^{-1}	No-slip moving wall
Tyre surface	20 km·h^{-1}	No-slip moving wall
Rim	20 km·h^{-1}/radius	No-slip rotating wall
Outlet	1 atm total pressure	Pressure outlet
AC	6960 m^3·h^{-1}	Mass flow inlet and outlet (ρ = 1.225 kg·m^{-3})
Bus	-	No-slip stationary wall
Walls of the wind tunnel	-	Symmetry condition

3. Results

From the solved models, the velocities and the drag forces (the magnitudes of the force components of the cruising direction exerted on the bus) (F_X) were assessed at 20 km·h^{-1} for three different geometries and induced flows.

3.1. Velocity Plots

To represent the typical flow patterns around the bus, velocity magnitudes were collected. The origin point of the coordinate system was the front plate of the bus, which was located on the ground and in the centre of the domain (see Figure 3). The velocity distribution on the X-Y plane was shown by the longitudinal midplane view. Figure 5 depicts the rear wake zones for the three bus types. The plane began after the rear plane of the bus at 12.5 m and ended 12 m further way, when the flow could be regarded as undisturbed. Velocities were normalized to the cruising speed of 20 km·h^{-1}. The peak velocity was 1.89, which developed at the frontal corners of the bus; this number was chosen as the maximum value of the scale. Figures for the visual comparison were taken at the sixty-second mark of the simulation flowtime.

The rear wake region length was roughly 2 m long in all the three models, yet additional shedding could also be observed. Since the shedding occurred stochastically, the velocity plots were not synchronized; thus, the comparison of the sizes of the wake structure could not be made. However, it can be noted that the upper recirculation bubble was larger in all three cases. The same was observed in some experimental measurements in the work of Lajos et al. [18], which was attributed to the moving ground. The most notable change that could be noticed is in Figure 5b; the recirculation bubble was roughly 0.25 m higher, due to the rear position of the AC, yet, in length it showed only a half-meter increase.

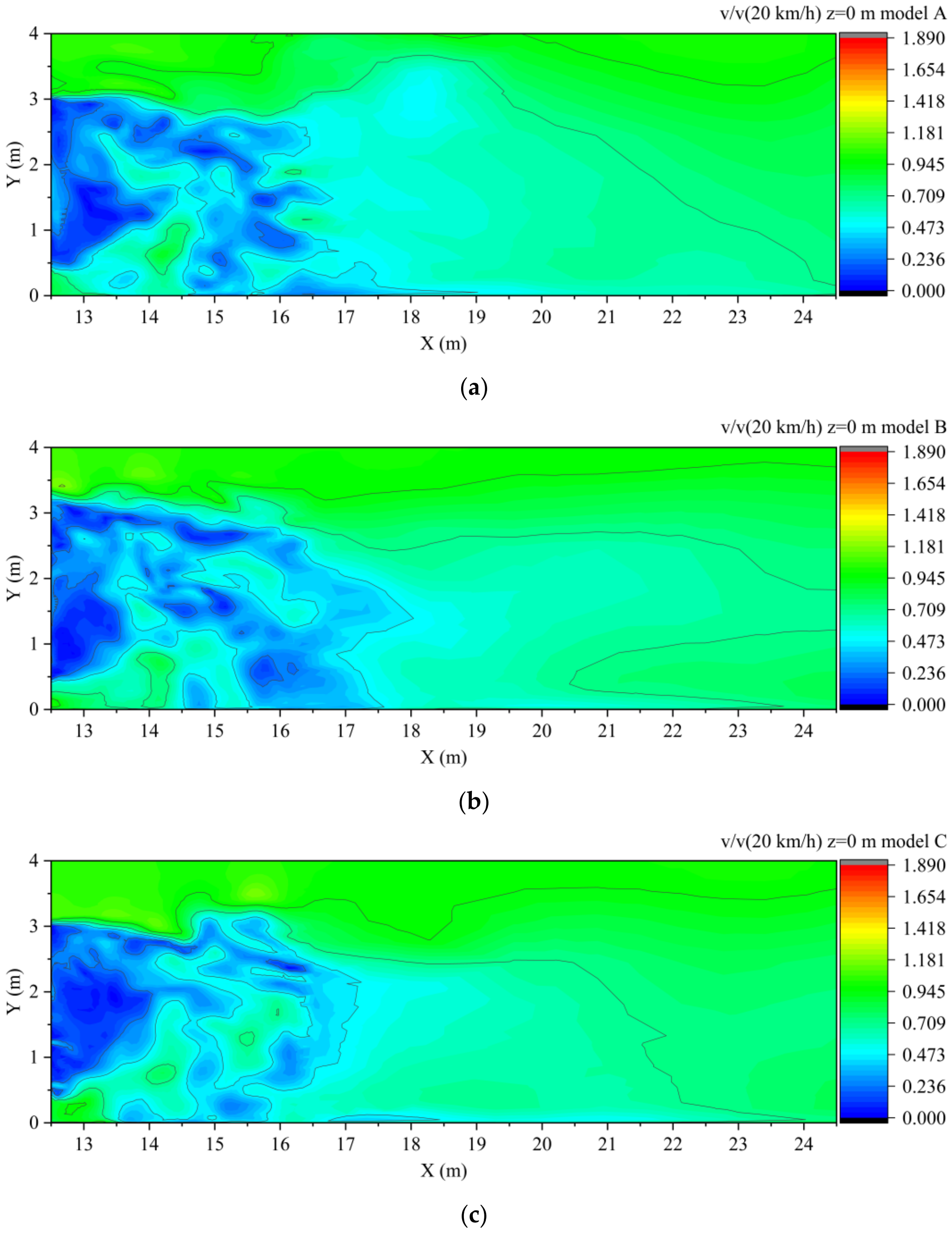

Figure 5. Longitudinal midsection velocity distribution for the rear wake region for (**a**) model A; (**b**) model B; (**c**) model C.

The AC had to be evaluated also, for additional comparison. When the AC was in the front, the wake region was shorter than when it was at the back (see Figure 6). The wake region behind the AC was steeper in the rear position, as shown in Figure 6b, because it was located at the tail end of the vehicle. In Figure 6a, a small stagnation point can be also seen on the leading edge, indicating that the frontal position could cause an upward induced drag. While there was no sign of stagnation in model B, the frontal circulation bubble of the AC was approximately half a metre larger. As numerous studies show [7], covering these wake regions may result in less drag loss. The reason for this disadvantageous shape could be flexibility and the small size of the AC. According to Figure 6, different shapes should be defined, depending on whether the AC is in the front or at the rear.

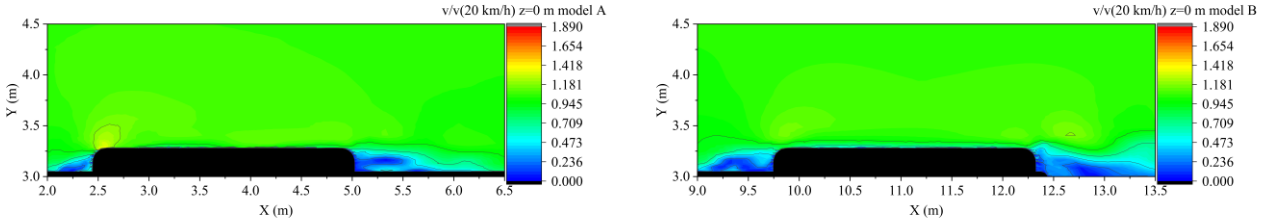

(**a**) (**b**)

Figure 6. Longitudinal midsection velocity distribution around the AC unit for (**a**) model A; (**b**) model B.

The wake region was also evaluated at three different Y-Z planes, at X = 12.5 m, 13 m, and 14 m, for the three models. The results of models A, B and C (Figure 7) were similar to the plots in Ref. [12].

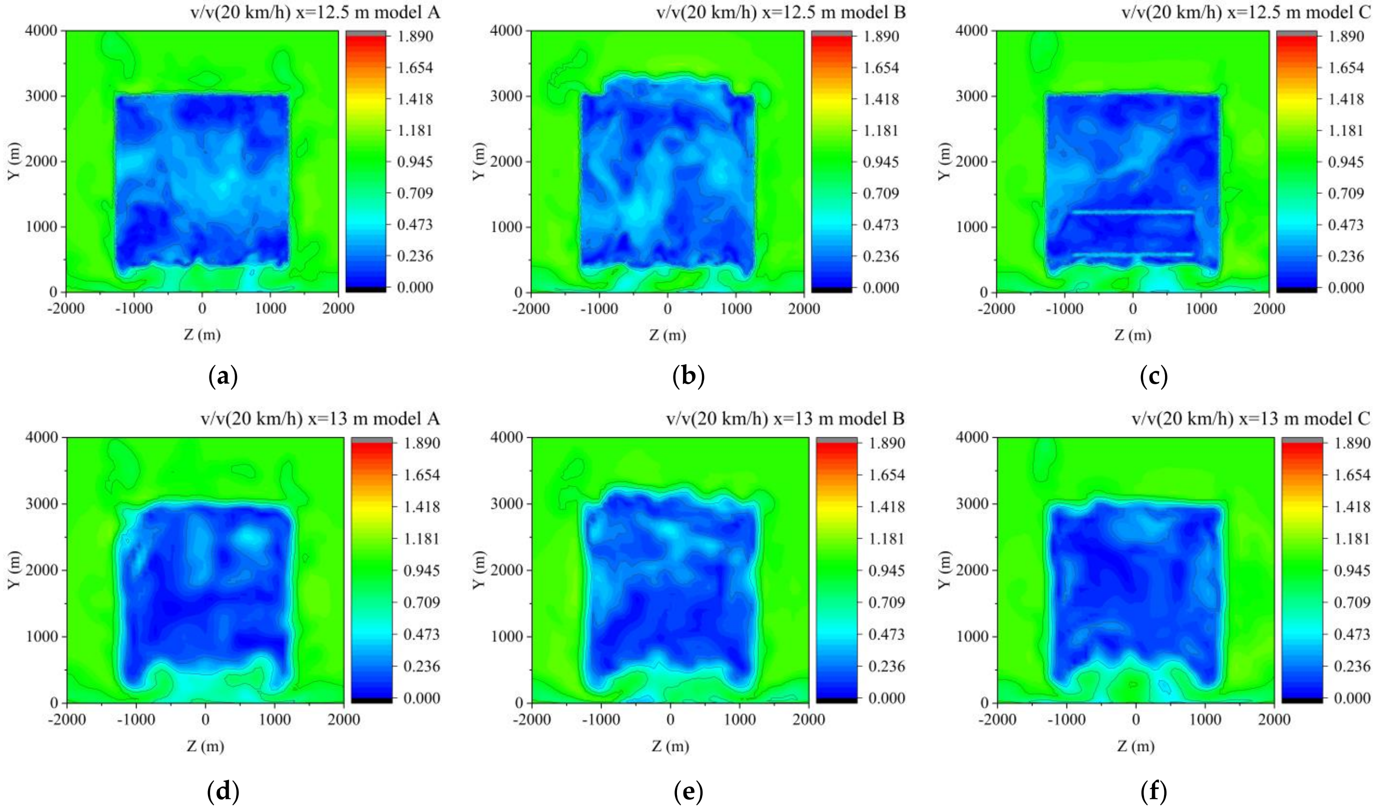

(**a**) (**b**) (**c**)

(**d**) (**e**) (**f**)

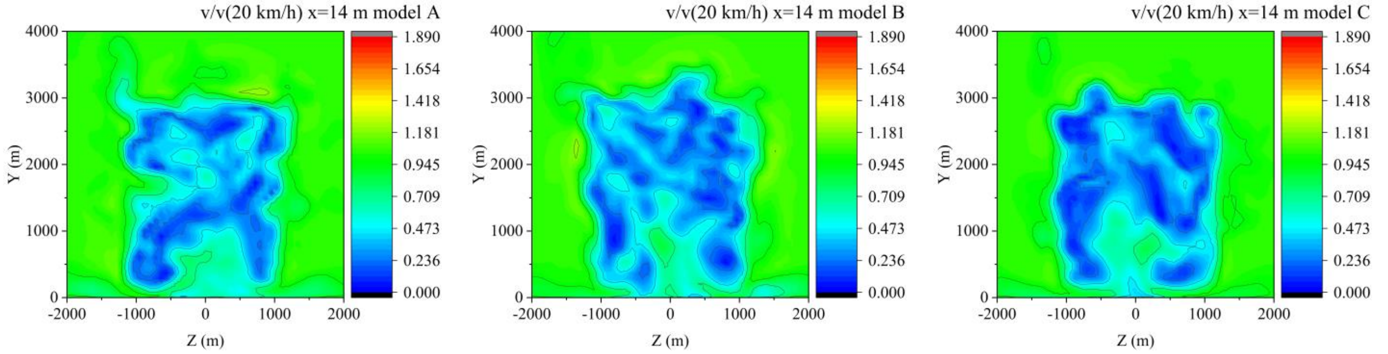

(**g**) (**h**) (**i**)

Figure 7. Vertical (Y-Z plane) velocity distribution for (**a**) model A at X = 12.5 m; (**d**) 13 m; (**g**) 14 m; (**b**) model B at X = 12.5 m; (**e**) 13 m; (**h**) 14 m; (**c**) model C at X = 12.5 m; (**f**) 13 m and (**i**) 14 m.

Figure 7a–c show the formation of longitudinal wakes. In Figure 7d–f, further development can be seen immediately after half a meter. After an additional 1 m, the rear wake region detached into four regions, as measured by particle image velocimetry (PIV) in the work of Gurlek et al. [19]. Figure 7c shows a slight distortion, with two bright lines at Y = 0.6 m and 1.2 m, which were attributed to the absence of prismatic layers at the AC outlets. However, this distortion only affected a small portion of the assessed area, and the effect become insignificant in Figure 7f.

To examine the symmetricity of the flow, horizontal (Z-X) planes were added at the height of the axis of the fan in model C (Y = 0.91 m). In all three models, it can be seen in Figure 8a,c,e that the flow slightly deformed towards the negative Z range (left-hand side of the bus). This asymmetric pattern could also be seen when the time-averaged drag force was assessed (see Figure 8b,d,f). It showed that the drag force on the left-hand side was noticeably larger than on the right-hand side. The difference between the mean values of both sides was greater than the standard deviation, indicating that the difference was noteworthy. It could be contributed to the following phenomena: by default, due to vortex shedding, a symmetric flow-pattern could not develop; an asymmetric pattern always develops with a bias to one side; due to the size differences of the mirrors, the flow was distorted. Because low velocity can produce unsteady flow patterns, visual assessment alone could not detect this bias. It would be preferable to use more time-samples or additional time-averaged values. Further time-samples were not shown, since the sheddings on Figure 8 were not synchronized.

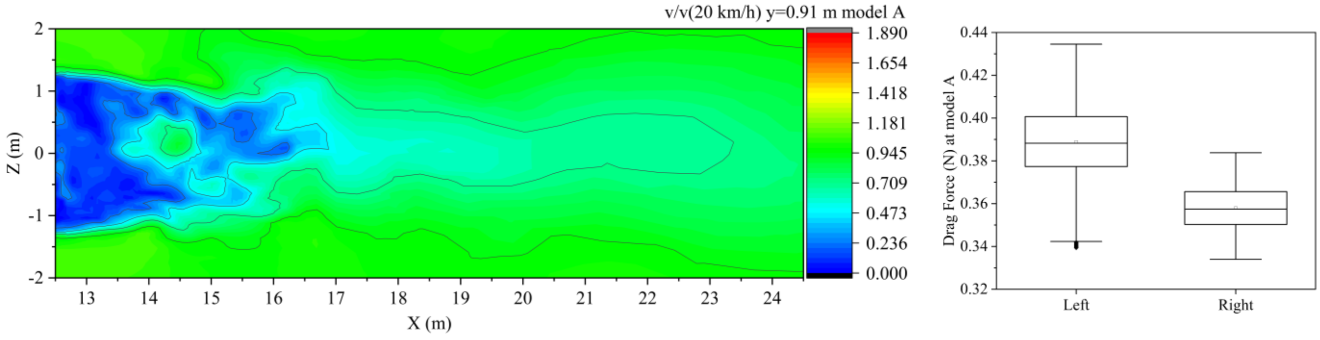

(**a**) (**b**)

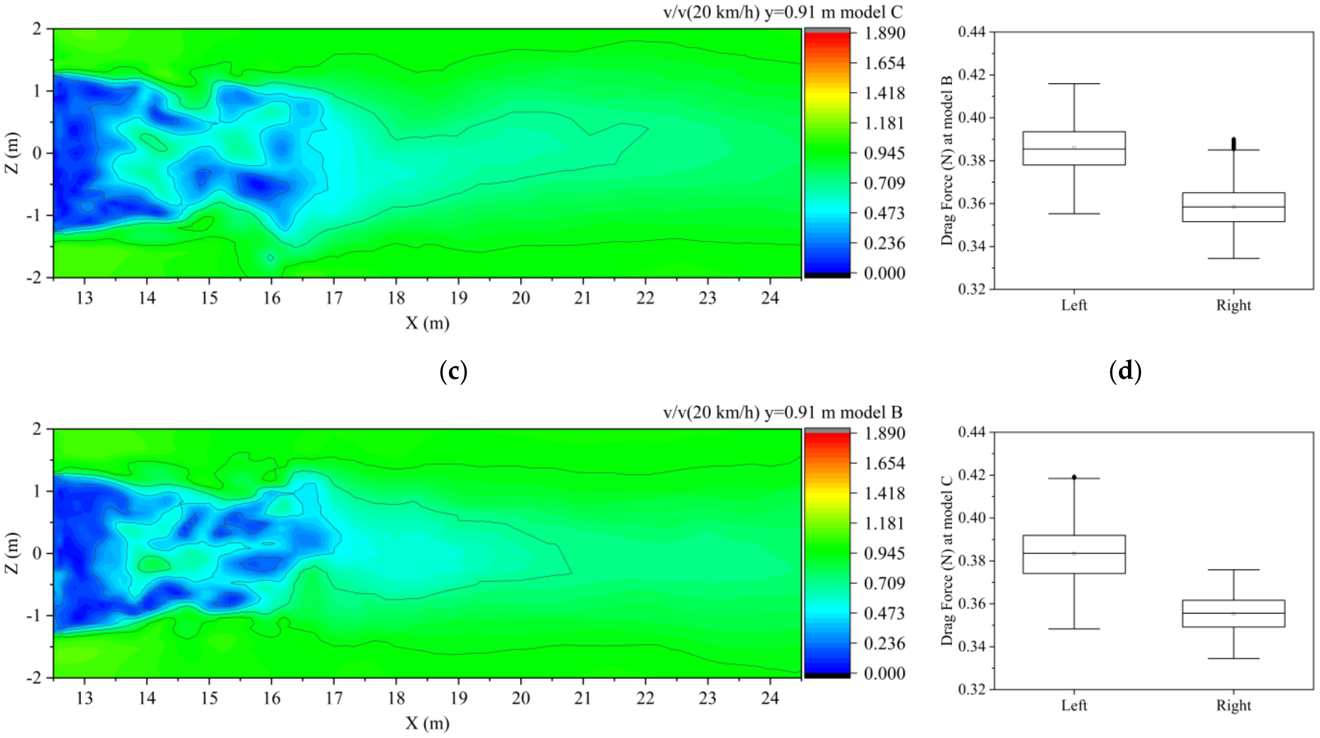

(**c**) (**d**)

(**e**) (**f**)

Figure 8. Horizontal (Z-X plane) velocity distribution for (**a**) model A at Y = 0.91 m; (**c**) model B at Y = 0.91 m; (**e**) model C at Y = 0.91 m and drag forces on the sides for (**b**) model A; (**d**) model B; (**f**) model C

3.2. Induced Flow Patterns

When the AC was turned on, all the three wake structures changed. Figure 9 depicts the disturbed wake regions for all three models. Because these were the most significant changes, minor changes in the flow structure were not examined. Comparing Figure 6a,b with Figure 9a,b, it could be seen that when it was placed on the top, a wake region formed. The height of this wake region was approximately 0.75 m, and it increased close to the trailing edge. The model A stagnation point was not visible, indicating that the induced flow near to the leading edge was able to reduce its magnitude. Figure 9a also shows that the frontal circulation bubble was reduced in size by half. When the AC was turned on, model B had a slightly longer circulation bubble compared to when it was off. In length, the wake region had similar dimensions. At approximately 1 m, the velocity started to build up again. This effect could indicate that the induced flow generated an induced drag; thus, aerodynamic losses could be expected in the case of model A and B, while in model C (see Figure 9c), when the fans were turned on, it disturbed the lower rear wake region. This disturbance reduced the lower recirculation bubble, and so a drag-loss reduction could be expected.

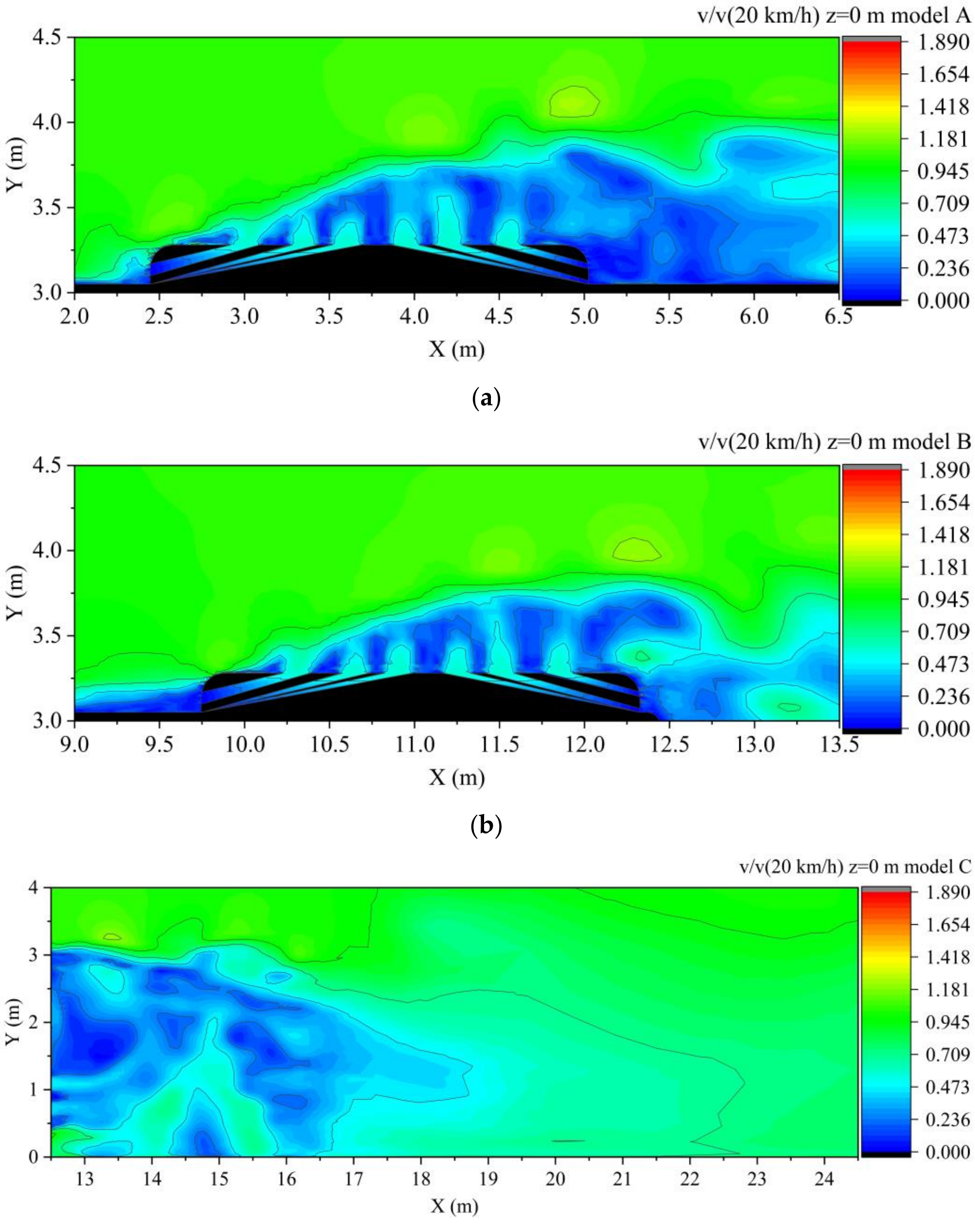

(**a**)

(**b**)

(**c**)

Figure 9. Distorted vertical flow patterns at the near AC region for (**a**) model A; (**b**) model B; (**c**) model C.

3.3. *Q-Criterion*

The Q-criterion [20] was used to depict the vortices, where Q was the second invariant of the velocity gradient tensor, S and Ω were the symmetric and antisymmetric parts of the tensor, respectively, and Q was expressed with Equation (1).

$$Q = 0.5 \cdot (\|S\|^2 + \|\Omega\|^2) \tag{1}$$

Model B was suitable to present the Q-criterion value formations at 90 s^{-2} in Figure 10. The cluster of hairpin vortices could be seen on the leading edges of the bus, which correspond to the results of Ref. [21]. The O-shaped vortices appeared as a result of the position of the AC inlets and outlets and of the flow. The growth trend was previously seen in Figure 9a,b, but the actual form can only be seen in Figure 10. During the literature search, no examples of these types of O-rings were discovered. They were only found when the O-ring formed on the rear surface [21]. This vortex dissipated as soon as it detached from the AC. Lastly, from Figure 10, large number of vortices can be seen forming around the side-view mirrors. Usually, vortices around mirrors are not evaluated directly, but a more relevant factor is the noise load caused by the increased velocities [22–24].

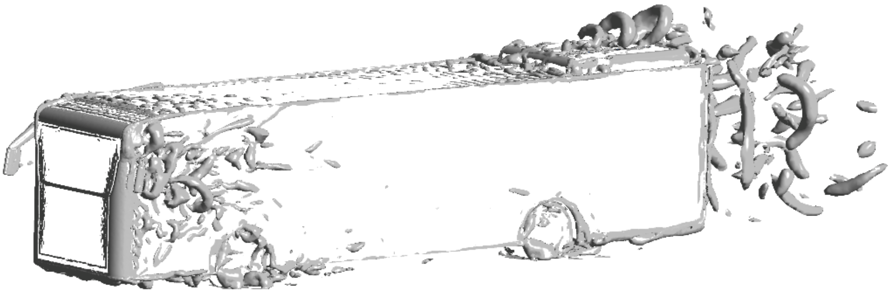

Figure 10. Value of 90 s^{-2} Q-criterion distribution for model B.

3.4. Force Values

The drag forces (Fx) were previously mentioned in Section 3.1, where the uneven distribution on the sides was noted. The Fx was the sum of the forces, yet the magnitude was low. The reason for this was that each individually investigated surface (e.g., left-hand and right-hand side) included peaking areas such as the trailing edges on the front, which reduced the Fx magnitudes on the sides or the roof. The same occurred on the front, where the Fx, caused by the stagnation pressure, was reduced by the same trailing edge.

Figure 11a depicts the frontal and rear surface Fx deviations. Because of the constant load from the wind-tunnel flow, the deviation on the frontal surface was smaller. The fluctuations could be caused by the right-hand side-view mirror, which was located on the front of the bus, and they could also be amplified by the corner vortices. On the rear end, the fluctuation was more noticeable. As previously stated in Section 3.1, shedding occurred. However, because it lacked a distinct pattern, comparing it with a wave function would have yielded low regression values.

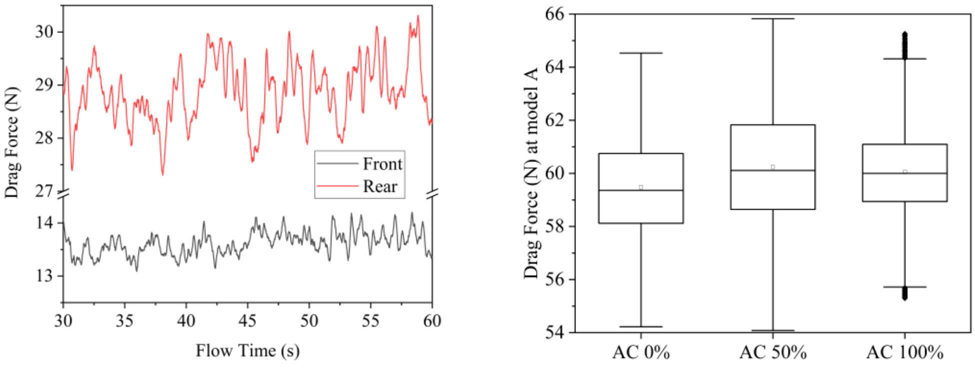

(**a**) (**b**)

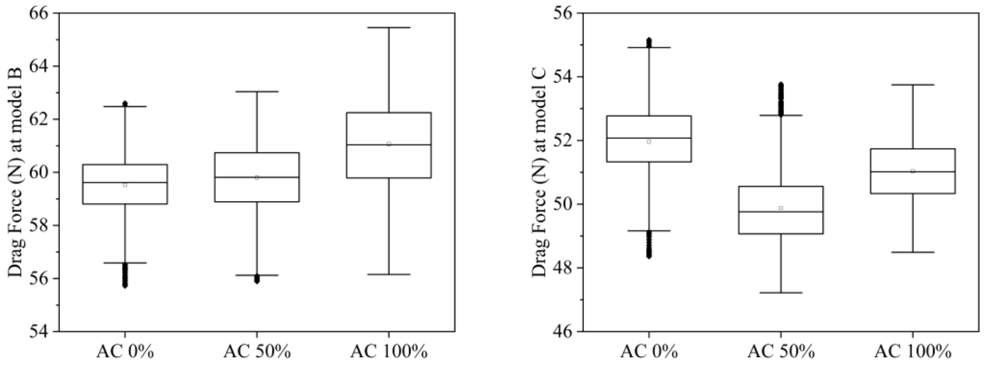

(**c**) (**d**)

Figure 11. F_X forces on (**a**) the front and rear of the bus; and (**b**) on the bus in model A; (**c**) model B; (**d**) model C.

The sum of F_X was obtained from the three models and at three different AC flow rates. Because at 20 km·h^{-1} relevant changes occurred rather than a time-averaged value, the mean and standard deviation should always be mentioned. When the AC was turned on, the baseline scenario (Figure 11b) showed a slight increase. This change could not be noticed, because of the deviation. The deviation at model B (see Figure 11c) become smaller, and the change was not noticeable when the AC was less than 50% of its maximum flow-rate. When it reached the maximum flow-rate, there was a noticeable increase. When the AC flow was induced, only model C had a decreased F_X (see Figure 11d). It was also worth noting that model C had the lowest F_X. The main reason for this could be that the AC was missing, and thus the wakes caused by it were absent.

3.5. Drag Coefficients

The best way to quantify aerodynamic losses was the application of drag coefficient (C_D), which was calculated using the following equation:

$$C_D = 2 \cdot F_X \cdot (A \cdot \rho \cdot v_c^2)^{-1} \tag{2}$$

where F_X was the sum of the force components, A was the projection area, v_c was the velocity of the bus in the cruising direction (20 km·h^{-1}), and ρ was the density of air (1.225 kg/m^3). Since the projected area could change when the AC was removed, the corresponding projected areas were used. When the projected area was kept at baseline, a pseudo change in drag loss occurred.

The C_D values showed that the AC flow rate had only a minor effect on the aerodynamic loss. It could also be concluded that removing the AC box (model C) resulted in a C_D reduction of at least 8%, and even more if the flow rate increased. This was the most significant change, because it was greater than the standard deviation. It was worth noting that the one-count drag reduction in model B is doubtful, because the C_D deviation was more than ten times greater than the improvement. According to the results in Table 4, the aerodynamic optimum at 20 km·h^{-1} was in the model C design at the 3480 m^3·h^{-1} flow rate, which resulted in a 12% C_D reduction compared with the baseline scenario.

Table 4. Drag coefficients for different geometry models and AC flow rates.

Drag Coefficients	Model A	Model B	Model C
AC 0% flow rate	0.395 ± 0.007 (base)	0.394 ± 0.013 (0%)	0.363 ± 0.008 (−8%)
AC 50% flow rate	0.396 ± 0.008 (0%)	0.399 ± 0.014 (1%)	0.348 ± 0.008 (−12%)
AC 100% flow rate	0.405 ± 0.011 (+3%)	0.398 ± 0.012 (1%)	0.356 ± 0.007 (−10%)

3.6. Validation

When one uses a 1:1 model, an experimental aerodynamic assessment of buses is difficult. In other cases, if the velocity is achievable, small-scale models can be used. Furthermore, at low speeds on a blunt body, shedding occurs, increasing the uncertainty of the measurement. As a result, because this paper only focuses on proposing an alternative position for the AC, only numerical models were used. Validation is divided into two parts: a flow pattern and a C_D comparison.

With the pure visual assessment [18,19] which had been made previously, the flow pattern described was similar to the result of this numerical study, including the shape of the rear wake region, the lower horseshoe vortices, and the clusters of hairpin vortices [21].

Because drag coefficients for buses are rarely investigated, only a few publications can serve as comparable data. Table 5 strengthens the fact that, as the speed of the vehicle decreases, so does the C_D [25]. At high speeds, in the case of buses, the C_D is usually relatively large, and these values are more acceptable for blunt bodies. However, in urban areas, where the average speed is lower [17], another C_D should be used. Furthermore, the use of a side-view mirror does not significantly change the C_D; the change is in the range of the standard deviation.

Table 5. Drag coefficients.

Drag Coefficient	Comment	Source
0.395 ± 0.007	20 $km \cdot h^{-1}$ with mirrors	Current study
0.389 ± 0.010	20 $km \cdot h^{-1}$ without mirrors	Previous study [12]
0.65	36 $km \cdot h^{-1}$	Cihan Bayındırlı [8]
0.43	80 $km \cdot h^{-1}$	Muthuvel et al. [14]
0.66	100 $km \cdot h^{-1}$	Hamit et al. [13]
0.65	120 $km \cdot h^{-1}$	Jadhav et al. [26]
0.41	modified	Jadhav et al. [26]

Based on independent numerical and experimental measurement, the current numerical results were in good agreement. However, limitations must be mentioned. Because the applied model was isothermal, it was assumed that the flow temperature from the AC had no significant effect on the flow rate, and did not generate flow structures. Because the numerical models were solved at a low speed, value fluctuations and unsteadiness affected the standard deviations of the examined indicators.

4. Discussion

Drag reduction can be solved by various methods, for example, with shape modification or by induced flows [7]. In the induced-flow method, the main objective was to disrupt the rear wake region by increasing the pressure in a low-pressure zone. For model A and B, drag reduction was not possible, since the flows generated wake regions and did not disrupt them. The induced flow for model A increased the drag area by approximately 3%.

When it comes to the energy efficiency of shape modification, the projected areas were required. By multiplying the drag-coefficient data from Table 4 with their corresponding projected areas, and assuming that the density and speed are constant, relative energy savings can be demonstrated, as shown in Table 6. A negative value indicates that it consumes more energy than the baseline and a positive value indicates that it saves energy. With the projected area correction, the relative energy savings for model C were approximately 4% greater than the drag change. Results shown in Table 6 made it clear that removing any large units from the roof could lead to an increase in energy efficiency. If the removal cannot be accomplished, further shape optimization would be required for the roof unit. The largest aerodynamic loss occurred when the AC was at the front, by approximately twice as much compared with when it was at the rear. However, the improvement in energy efficiency was roughly the same magnitude as the loss, which was approximately 2%.

Table 6. Relative energy savings for different geometry models and AC flow rates.

Relative Energy Saving	Model A	Model B	Model C
AC 0% flow rate	baseline	0.1%	12.7%
AC 50% flow rate	−0.5%	−1.2%	16.2%
AC 100% flow rate	−2.6%	−0.9%	14.3%

The results can be expressed with nondimensional values, if the Reynolds number ratio of AC to wind tunnel is used (Re_{AC}/Re_{W}).

$$Re_{AC}/Re_W = v_{AC} \cdot D \cdot (v_c \cdot H)^{-1} \tag{3}$$

where v_{AC} is the flow velocity from the AC, and D is the hydraulic diameter of the AC unit. At 50% of the capacity, Re_{AC}/Re_{W} is 0.26, and at 100%, Re_{AC}/Re_{W} is 0.53 for model B. At 0.26 Re_{AC}/Re_{W}, the reduction in drag is 4%, while at 0.53 it is 2%. In practice, it is not recommended that this flow rate should be increased, due to the increase in ventilation power demand, but with more advanced heat exchangers this flow rate should be decreased.

Firstly, the AC cannot be freely positioned on the rear surface of the bus; the bus must let in as much light as possible, so placing it higher may limit this possibility.

Secondly, concentrating the apparatuses at the bottom makes the bus more stable. However, the fact that the rotating blades are at the pedestrian level, raises safety concerns. Of course, finer grills could be used to solve the problem, but this would increase the ventilation work.

Thirdly, the use of side-view mirrors in numerical models can be questioned in this scenario, because the drag coefficient changes and the flow structure deforms significantly. However, the change in C_D is within the standard deviation, and consequently the lack of mirrors does not result in a significant difference.

5. Conclusions

The flow structures and drag forces obtained from large eddy simulations of three different shapes of bus cruising at 20 km·h^{-1} were analysed in the presented work.

- Flow representation shows that the side-,wind mirror created vortices, but in drag losses, these could be ignored because the difference was within the error range.
- When the fans of the external unit of the air conditioner were activated, O-rings appeared and quickly dissipated.
- The constant flow induced by the external unit of the air conditioner on the roof had a minor increasing effect on drag loss, if it existed at all.
- Drag loss was reduced when the steady flow was induced in the rear of the bus.
- The steady-flow drag-reduction optimum was found to be at 0.26 Re_{AC}/Re_{W}.
- According to the results, placing the box of the external unit in the rear end could result in an 8% drag reduction, meaning a 12.7% energy saving could be realised.

Funding: This research was financed by the Thematic Excellence Programme of the Ministry for Innovation and Technology in Hungary (ED_18-1-2019-0028), within the framework of the (Automotive Industry) thematic programme of the University of Debrecen.

Data Availability Statement: Not applicable.

Acknowledgements: The author expresses appreciation to DKV Ltd. for their kind help.

Conflicts of Interest: The author declares no conflict of interest.

References

1. Bilgili, M.; Aktas, A.E.; Cardak, E. Thermodynamic Analysis of Bus Air Conditioner Working with Refrigerant R600a. *Eur. Mech. Sci.* **2017**, *1*, 69–75. https://doi.org/10.26701/ems.321874.
2. Sylla, F.K.; Faye, A.; Diaw, M.; Fall, M.; Tal-Dia, A. Traffic Air Pollution and Respiratory Health: A Cross-Sectional Study among Bus Drivers in Dakar (Senegal). *Open J. Epidemiol.* **2018**, *8*, 81699. https://doi.org/10.4236/ojepi.2018.81001.
3. Shen, Y.; Li, C.; Dong, H.; Wang, Z.; Martinez, L.; Sun, Z.; Handel, A.; Chen, Z.; Chen, E.; Ebell, M.H.; et al. Community Outbreak Investigation of SARS-CoV-2 Transmission among Bus Riders in Eastern China. *JAMA Intern. Med.* **2020**, *180*, 1665–1671. https://doi.org/10.1001/jamainternmed.2020.5225.
4. Zhang, Z.; Han, T.; Yoo, K.H.; Capecelatro, J.; Boehman, A.L.; Maki, K. Disease transmission through expiratory aerosols on an urban bus. *Phys. Fluids* **2021**, *33*, 015116. https://doi.org/10.1063/5.0037452.
5. Gilliéron, P.; Kourta, A. Aerodynamic drag control by pulsed jets on simplified car geometry. *Exp. Fluids* **2013**, *54*, 1457. https://doi.org/10.1007/s00348-013-1457-y.
6. Tounsi, N.; Mestiri, R.; Keirsbulck, L.; Oualli, H.; Hanchi, S.; Aloui, F.; Algiers, E.M.P.O.; Leste, N.D.D.M. Experimental study of flow control on bluff body using piezoelectric actuators. *J. Appl. Fluid Mech.* **2016**, *9*, 827–838. https://doi.org/10.18869/acadpub.jafm.68.225.24488.
7. Szodrai, F. Quantitative Analysis of Drag Reduction Methods for Blunt Shaped Automobiles. *Appl. Sci.* **2020**, *10*, 4313. https://doi.org/10.3390/app10124313.
8. Bayındırlı, C. Drag reduction of a bus model by passive flow canal. *Int. J. Energy Appl. Technol.* **2019**, *6*, 24–30. https://doi.org/10.31593/ijeat.533745.
9. Pastoor, M.; Henning, L.; Noack, B.R.; King, R.; Tadmor, G. Feedback Shear Layer Control for Bluff Body Drag Reduction. *J. Fluid Mech.* **2008**, 608, 161–196. https://doi:10.1017/S0022112008002073.
10. Aubrun, S.; McNally, J.; Alvi, F.; Kourta, A. Separation flow control on a generic ground vehicle using steady microjet arrays. *Exp. Fluids* **2011**, *51*, 1177–1187. https://doi.org/10.1007/s00348-011-1132-0.
11. Littlewood, R.P.; Passmore, M.A. Aerodynamic drag reduction of a simplified squareback vehicle using steady blowing. *Exp. Fluids* **2012**, *53*, 519–529. https://doi.org/10.1007/s00348-012-1306-4.
12. Szodrai, F. Numerical Assessment of Side-Wind Effects on a Bus in Urban Conditions. *Appl. Sci.* **2022**, *12*, 5688. https://doi.org/10.3390/app12115688.
13. Hamit, S.; Yakup, İ. Drag Coefficient Determination of a Bus Model Using Reynolds Number Independence. *Int. J. Automot. Eng. Technol.* **2015**, *4*, 146–151.
14. Muthuvel, A.; Murthi, M.K.; Sachin, N.P.; Koshy, V.M.; Sakthi, S.; Selvakumar, E. Aerodynamic Exterior Body Design of Bus. *Int. J. Sci. Eng. Res.* **2013**, *4*, 2453–2457.
15. Roache, P.J. Perspective: A method for uniform reporting of grid refinement studies. *ASCE J. Fluids Eng.* **1994**, *116*, 405–413.
16. Nicoud, F.; Ducros, F. Subgrid-scale stress modelling based on the square of the velocity. *Flow Turbul. Combust.* **1999**, *62*, 183–200. https://doi.org/10.1016/j.jcp.2004.10.018.
17. Vámosi, A.; Czégé, L.; Kocsis, I. Development of Bus Driving Cycle for Debrecen on the Basis of Real-traffic Data. *Period. Polytech. Transp. Eng.* **2022**, *50*, 184–190. https://doi.org/10.3311/pptr.16109.
18. Lajos, T.; Preszler, L.; Finta, L. Effect of moving ground simulation on the flow past bus models. *J. Wind Eng. Ind. Aerodyn.* **1986**, *22*, 271–277. https://doi.org/10.1016/0167-6105(86)90090-5.
19. Gurlek, C.; Sahin, B.; Ozkan, G.M. PIV studies around a bus model. *Exp. Therm. Fluid Sci.* **2012**, *38*, 115–126. https://doi.org/10.1016/j.expthermflusci.2011.11.014.
20. Hunt, J.C.R.; Wray, P.M.A.A. Eddies, Stream, and Convergence Zones in Turbulent Flows. In *Center for Turbulence Research, Proceedings of the Summer Program*; 1988; pp. 193–208. Available online: https://web.stanford.edu/group/ctr/Summer/201306111537.pdf (accessed on 28 October 2022).
21. Krajnović, S.; Davidson, L. Numerical study of the flow around a bus-shaped body. *J. Fluids Eng. Trans. ASME* **2003**, *125*, 500–509. https://doi.org/10.1115/1.1567305.
22. Zhu, J.J.; Liu, G.W. Numerical optimization for aerodynamic noises of rear view mirrors of vehicles based on rectangular cavity structures. *J. Vibroeng.* **2018**, *20*, 1240–1256. https://doi.org/10.21595/jve.2017.18740.
23. Chu, Y.J.; Shin, Y.S.; Lee, S.Y. Aerodynamic analysis and noise-reducing design of an outside rear view mirror. *Appl. Sci.* **2018**, *8*, 519. https://doi.org/10.3390/app8040519.
24. Chode, K.K.; Viswanathan, H.; Chow, K. Noise emitted from a generic side-view mirror with different aspect ratios and inclinations. *Phys. Fluids* **2021**, *33*, 084105. https://doi.org/10.1063/5.0057166.
25. Janna, W.S.; Schmidt, D. Fluid Mechanics Laboratory Experiment : Measurement of Drag on Model Vehicles. In Proceedings of the ASEE Southeast Section Conference, 2014. Available online: http://se.asee.org/proceedings/ASEE2014/Papers2014/4/11.pdf (accessed on 28 October 2022).
26. Jadhav, C.R.; Chorage, R.P. Modification in commercial bus model to overcome aerodynamic drag effect by using CFD analysis. *Results Eng.* **2020**, *6*, 100091. https://doi.org/10.1016/j.rineng.2019.100091.